Korean J. Chem. Eng., 40(1), 67-78 (2023)
DOI: 10.1007/s11814-022-1339-1

pISSN: 0256-1115
eISSN: 1975-7220

Different modes of bubble migration near a vertical wall in pure water

Runze Cai*,, Enbo Ju*,**, Wenyi Chen*,**,†, and Jiao Sun*,**,***,†**

*Department of Process Equipment and Control Engineering, Hebei University of Technology, Tianjin 300130, China
**National-Local Joint Engineering Laboratory for Energy Conservation in Chemical Process Integration and Resources Utilization, School of Chemical Engineering, Hebei University of Technology, Tianjin 300130, China
***Department of Mechanics, School of Mechanical Engineering, Tianjin University, Tianjin 300350, China
(*Received 14 June 2022 • Revised 29 September 2022 • Accepted 6 November 2022*)

Abstract−The migration of deformable bubbles with different sizes near a vertical wall in pure water was experimentally studied by the dual-camera orthogonal shadow method. The key factors affecting the migration are discussed. It was found that the effect of size and initial distance on bubble migration is indirect. For bubbles of the same diameter (d_{eq}=3.10 mm), the same mode occurs when the initial distance ($0.5 \le L^* \le 3.5$) is changed. When the initial distance (L^*=0.5) is constant, the same mode appears for bubbles of different sizes (2.27 mm≤d_{eq}≤3.40 mm). Furthermore, different modes are found in the same initial distance (L^*=0.5) and size (d_{eq}=3.10 mm). In fact, the migration mode is determined by the initial distance, Reynolds number and Weber number. The size and initial distance can influence the frequency of different modes. Considering a variety of factors, four basic migration modes are summarized. New correlations are proposed to predict bubble behavior in different modes near the wall. The kinematic and dynamic parameters of different modes are discussed. It is expected that the results can be helpful to predict the gas-liquid flow near a wall and to improve related heat and mass transfer process.

Keywords: Bubble Migration, Wall Effect, Dynamics, Multiphase Flow, Bubble Behavior

INTRODUCTION

Bubbles and bubbly flow have long been of great interest in chemical engineering. The characteristics of rising bubbles, such as velocity, size, distribution, and forces acting on the bubbles, are critical to heat and mass transfer [1-3]. There have been substantial studies on bubbles with different behaviors in an infinite liquid. The relationship of bubble size, velocity and trajectory has been studied [4-7]. The influence of the wall on the bubbles has also received extensive attention [8-13].

A typical method to evaluate the bubble behavior near a wall is to use the dimensionless initial distance (L^*) as a key parameter, which is the ratio of the distance from the initial centroid of the bubble and the wall to the equivalent radius of the bubble. de Vries [14] observed the rising behaviors of small bubbles with different sizes (less than 1 mm in diameter) near the wall. According to the differences of the initial distance and the bubble size, various bubble rising trajectories were observed, such as sliding along the wall, bouncing up along the wall, separating from the wall after bouncing once, and bouncing up with larger amplitude. Moctezuma et al. [15] studied the influence of the dimensionless initial distance on the rising trajectory and the speed of bubbles of different sizes. The frequency of bubble collision with the wall decreased with the increase of the initial distance, due to the decrease of the wall inducing lift and other hydrodynamic forces. That is, the wavelength of the bubble rising trajectory increased with the increase of the initial distance. The average velocity of the bubbles decreased first and then increased with the increase of the initial distance. Jeong et al. [16] studied the influence of the initial distance and wall material on the rising behavior of bubbles. When $L^* \le 2$, the influence of the wall material was more significant, which was specifically manifested as the change in the trajectory of the bubble. When $L^* > 2$, the change was weakened. Lee et al. [17] analyzed the influence of the initial distance on the bubble trajectory and the wake structure. When L^*=0.3, the bubble collided with the wall, and the original vortex in the bubble wake could produce a secondary vortex pair with opposite signs under the effect of the wall. With the increase of the initial distance, when L^*=0.9, the bubbles no longer collided with the wall, and the wall still had a significant influence on the wake structure. When L^*=1.9, the influence of the wall on the wake structure was further weakened. Chen et al. [18] studied the influence of the initial distance and different porosity of wire mesh on bubble behavior. It was found that the energy loss of the near-mesh bubble was significantly smaller than that of the impermeable wall. For denser meshes, energy dissipation was not related to L^*.

The importance of initial distance is indisputable. However, as a deformable particle, the behavior of a rising bubble is complicated. In this work, the dual-camera orthogonal shadow method is used to measure the bubble migration. For the unbounded situation, a single camera is often used to capture the bubble motion. Considering the wall effect, the bubble motion along the wall normal direction and the wall spanwise direction is different, and the complete bubble motion can be collected in three dimensions by using this method. The results show that the bubble behavior is not only related to the dimensionless initial distance but also to the bubble size. Note that the effects of size and initial distance on bubble migration are

†To whom correspondence should be addressed.
E-mail: cwy63@126.com, sunjiao2007@163.com

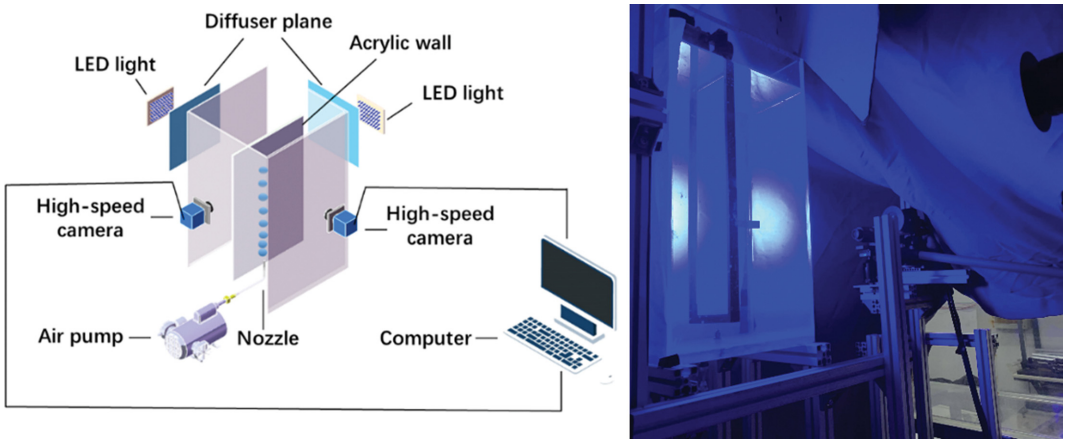

Fig. 1. Experimental setup.

indirect. The migration mode is determined by the dimensionless initial distance, Reynolds number and Weber number. Considering a variety of factors, four basic migration modes are summarized. New correlations are proposed to predict bubble migration in different modes near the wall. The kinematic parameters and dynamics of bubbles in different modes are discussed.

MATERIAL AND METHODS

1. Experimental Setup

The experimental apparatus is shown in Fig. 1: The left is the schematic diagram, the right is the actual photo. It consists of a rectangular acrylic container, an acrylic wall (with a no-slip boundary condition at the surface), two CCD cameras, a LED lamp with a wavelength of 380 nm and another LED lamp with a wavelength of 450 nm. The size of the container is 300 mm×300 mm×650 mm. The size of the wall is 580 mm×200 mm×20 mm. Deionized water is used. The experimental environment temperature is 19.8 °C, the density of the liquid (ρ_l) is 998.4 kg/m^3, the density of the gas (ρ_g) is 1.206 kg/m^3, the surface tension (σ) is 0.073 N/m, and the viscosity (μ) is 1.008×10^{-3} Pa·s. The needle nozzle is fixed at the bottom of the container. A miniature air pump is used as the gas source to provide air. A trace gas flow regulating valve is used to adjust the bubble frequency. The interval between two bubbles is about 17 s to avoid the interference of the previous bubble wake to the next bubble. Two vertically placed cameras are used. The camera acquisition frequency is 180 Hz. The resolution of camera 1 is 15.67 pixels/mm. The resolution of camera 2 is 15.25 pixels/mm. The coordinate origin (0, 0, 0) is 300 mm above the needle nozzle exit (the initial position of the bubble).

The initial distance (L) is defined as the distance from the center of the needle nozzle to the wall, as shown in Fig. 2. The initial distance is controlled by a lead screw with a precision of 0.1 mm. The lead screw is fixed perpendicular to the wall, which ensures that the wall spanwise direction is maintained during the experiment. The initial distance is dimensionless (L^*) as

$$L^* = 2L/d_{eq} \quad (1)$$

where d_{eq} is the equivalent diameter of the bubble. Its calculation

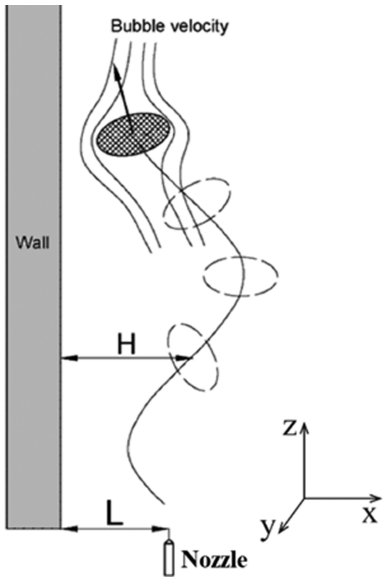

Fig. 2. The bubble migration under the wall effect.

formula is

$$d_{eq} = \sqrt[3]{d_h^2 d_v} \quad (2)$$

where d_h and d_v are the horizontal axis and the vertical axis, respectively. Five kinds of bubbles of different sizes (d_{eq}=2.27 mm, 2.49 mm, 2.89 mm, 3.10 mm, 3.40 mm) are obtained by changing the types of the needles. There are twelve conditions according to the different initial distances (L^*=0.5, 1.29, 1.94, 2.58, 3.23, 3.87, 4.52, 5.16, 5.81, 6.45, 7.74, 8.39). Each condition was measured 100 times.

2. Image Processing Methods and Measurement Uncertainty

Image processing is used to extract the feature parameters, including bubble contours, major and minor axis lengths, and centroid coordinates. Fig. 3 shows the corresponding results of the original image after the image processing. Noise may appear during the image acquisition, such as uneven image background gray scale, inconspicuous contrast between bubbles and background, and blurred edges of bubbles. It will reduce the accuracy of the bubble

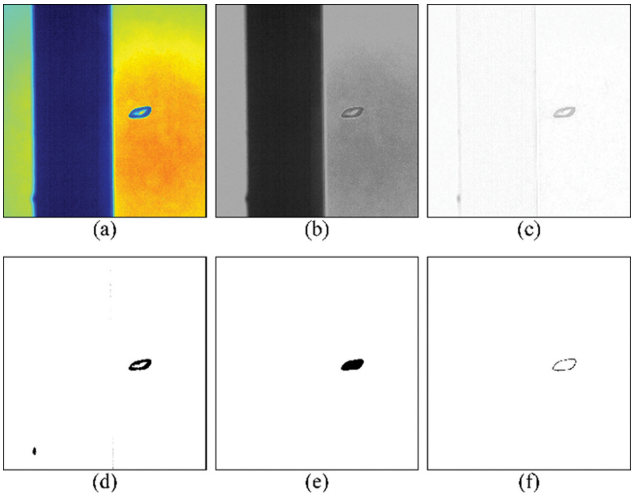

Fig. 3. Image processing: (a) original image (b) preprocessing (c) background removal (d) low-pass filter and binarization (e) bubble center filling and median filter (f) edge detection.

detection. Image preprocessing can reduce the influence of noise on the bubble detection, as shown in Fig. 3(b). The vertical wall affects the bubble detection. Fig. 3(c) is background removal, which removes the effect of walls on bubble detection. In the image process, the noise is mainly concentrated in the high-frequency part. A low-pass filter is used to effectively suppress high-frequency components and pass low-frequency components smoothly to filter out noise in the neighborhood. Then the image is binarized by threshold segmentation. The difference between the target image and the background is used to select an appropriate threshold to obtain a clear bubble contour, as shown in Fig. 3(d). Fig. 3(e) is a complete and clear bubble image obtained by the hole filling function combined with the median filter function. Fig. 3(f) shows the final bubble contour obtained by the edge detection function. The relevant feature parameters are extracted through the fitting function. According to the relationship between bubble displacement and the time interval obtained through processing, the local velocity components u_x, u_y, and u_z of the bubble along the x, y, and z coordinate axes, respectively, can be calculated as:

$$u_{ix}=\frac{x_i-x_{i-1}}{\Delta t},\ u_{iy}=\frac{y_i-y_{i-1}}{\Delta t},\ u_{iz}=\frac{z_i-z_{i-1}}{\Delta t} \tag{3}$$

where (x_i, y_i, z_i) and $(x_{i-1}, y_{i-1}, z_{i-1})$ are the centroid coordinates of the bubbles in the subsequent two frames, Δt is the time interval, and the x, y, z coordinate axes are along the wall normal direction, the wall spanwise direction, and the flow direction, respectively, as shown in Fig. 2. The local velocity (u_i) of the bubble can be calculated as:

$$u_i=\sqrt{u_{ix}^2+u_{iy}^2+u_{iz}^2} \tag{4}$$

According to previous research, the uncertainty of the measurement is mainly caused by two factors. The first is digital image processing errors. In this study the resolution ratio is 2,048×2,048 pixels, and the lens coverage is 130×130 mm. When a bubble does not collide with the wall, the maximum error of bubble edge detection is ±1 pixel. The maximum uncertainty of bubble diameter is less than 3%. When bubbles collide with walls, the maximum error of bubble edge detection is ±2 pixels. The uncertainty of bubble diameter is less than 5%. The second factor is the limited number of points available for averaging. In this paper, the time interval between two consecutive frames is 12 ms, so the impact can also be ignored.

RESULTS AND DISCUSSION

1. The Key Factors Affecting the Bubble Migration Near the Wall

As mentioned, L^* is usually used in previous studies as the key factor to evaluate the near-wall bubble behavior [15-19]. However, the effect of the L^* is complicated. For different L^*, the bubbles may have similar behaviors. Moreover, bubbles of the same L^* may display different styles, which will be discussed in Section 3.2.

In previous studies, the bouncing of bubbles along the wall usually occurs with a small L^* [14,16,18]. In the current work, this also happens when L^* is larger. Fig. 4 shows the same size bubbles (d_{eq}= 3.10 mm) rising with the similar behavior at different L^*. This kind of similar behavior is considered the same mode. In this mode, all bubbles are observed to bounce along the wall. All these processes show a high similarity, and are defined as Mode 1. The criterion of collision between the bubble and the wall is the value of the dimensionless distance between the bubble centroid and the wall, and the same criterion has been used by Takemura and Magnaudet [20]. It is defined as

$$H^*=2H/d_{eq} \tag{5}$$

where the H is the distance between the bubble centroid and the wall as shown in Fig. 2.

To quantitatively compare the bubble migration near a wall at different L^*, the relevant parameters are calculated and the results are shown in Table 1. L^* is the dimensionless initial distance; $\overline{\lambda}^*$ is the average dimensionless trajectory wavelength; $\overline{h}^*$ is the average dimensionless trajectory amplitude; $\overline{d}_{eq}$ is the average equivalent diameter of the bubble; $\overline{Re}$ is the average Reynolds number; $\overline{We}$ is the average Weber number; $\overline{u}$ is the average velocity of the bubble. The dimensionless trajectory wavelength (λ^*) can be calculated by:

$$\lambda^*=2\lambda/d_{eq} \tag{6}$$

The dimensionless trajectory amplitude (h^*) can be calculated by:

$$h^*=2h/d_{eq} \tag{7}$$

The Reynolds number (Re) can be calculated by:

Table 1. Parameters of bubble migration under different L^*

L^*	$\overline{\lambda}^*$	$\overline{h}^*$	$\overline{d}_{eq}$	$\overline{Re}$	$\overline{We}$	$\overline{u}$
0.50	10.75	1.97	3.1	794.14	2.88	0.26
1.29	10.81	1.96	3.1	792.00	2.86	0.26
1.94	10.76	1.97	3.1	792.87	2.88	0.26
2.58	10.94	1.99	3.1	794.62	2.89	0.26
3.23	10.78	1.95	3.1	797.93	2.91	0.26

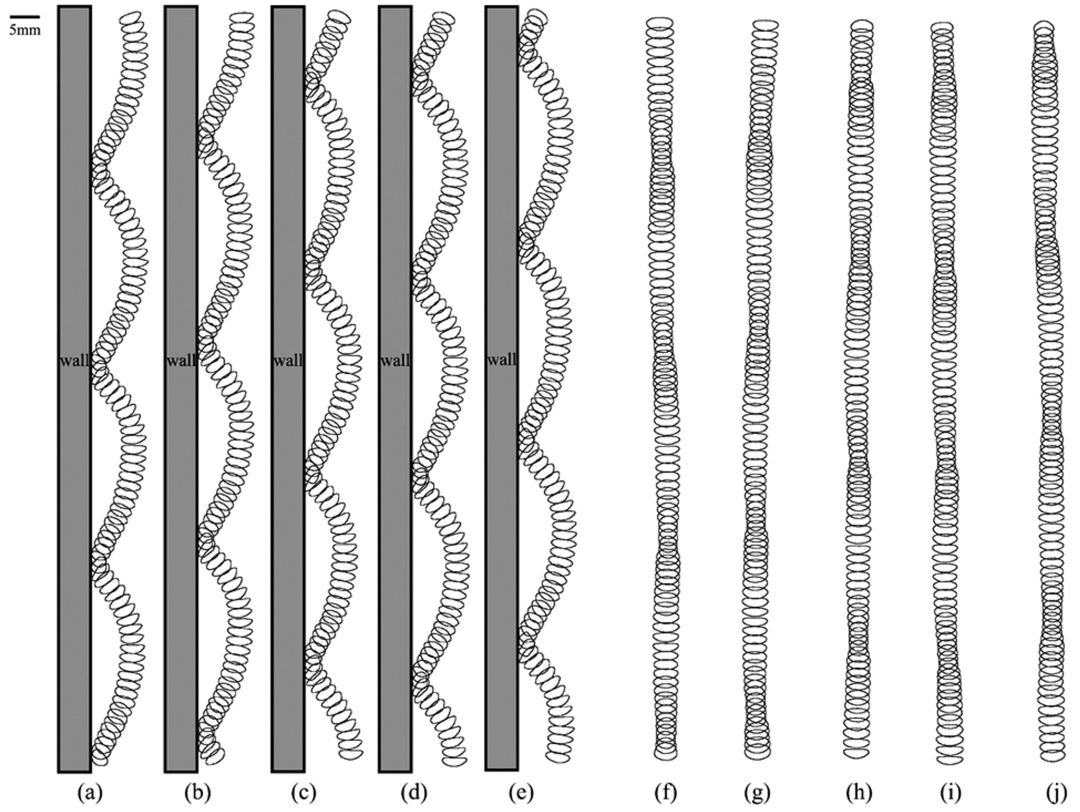

Fig. 4. Bubble migration in the same mode with different L^*. (a)-(e) the results in x-z plane, (f)-(j) the results in y-z plane. For (a) and (f), L^*=0.50; (b) and (g), L^*=1.29; (c) and (h), L^*=1.94; (d) and (i), L^*=2.58; (e) and (j), L^*=3.23. The scale bar is in the top left of the figure.

$$Re = \rho_l u d_{eq} / \mu_l \quad (8)$$

The Weber number (We) can be calculated by

$$We = \rho_l u^2 d_{eq} / \sigma \quad (9)$$

With the increase of L^*, there is no obvious change in the various parameters, and the repeatability error is within 0.1%. This result shows that the L^* is just one of the factors affecting the bubble migration near a wall in the current work. For the same-size bubbles rising in the same mode, the L^* does not affect other parameters, but it can affect the frequency of different modes. This part will be explained in section 3.2.

Previous studies pointed out that as the bubble size increases, the motion of unbounded bubbles changes from one-dimensional (straight line) to two-dimensional (zigzag) and finally to three-dimensional (spiral) [14,15,21]. To investigate the influence of the size on bubble migration near a wall, the bubble migration on the same L^* with different d_{eq} was compared. The results show that the size of bubbles can affect the bubble rising near a wall. Interestingly, the effect of size on bubble migration near the wall is not as direct as that on the unbounded bubbles, which is the same as the effect of the initial distance. At the same L^*, bubbles of different sizes may have similar behavior. Moreover, bubbles of the same size may display different styles, which will be discussed in Section 3.2.

Fig. 5 shows that the bubbles with different sizes rise at the same L^* (L^*=0.50). What they have in common is that all bubbles bounce along the wall. And the relevant parameters are shown in Table 2.

Table 2. Parameters of bubble migration in the same mode with different sizes

$\bar{d}_{eq}$	$\bar{\lambda}^*$	$\bar{h}^*$	$\bar{Re}$	$\bar{We}$	$\bar{u}$
2.27	15.23	2.67	619.13	2.43	0.28
2.49	15.12	2.53	666.93	2.56	0.27
2.89	12.46	2.25	759.82	2.84	0.27
3.10	10.75	1.97	794.14	2.88	0.26
3.40	10.08	1.80	859.62	3.07	0.26

As the bubble size increases, the $\bar{\lambda}^*$, $\bar{h}^*$ and $\bar{u}$ decrease while the $\bar{Re}$ and $\bar{We}$ increase. Analyzing the velocity components and forces of bubbles with different sizes, it is found that there is a high similarity among them. The details of the analysis are in section 3.3 and 3.4.

2. Different Modes of Bubble Migration Near the Wall

The complicated influence of the L^* and bubble size on bubble migration near the wall has been discussed in Section 3.1, including that bubbles of the same size may rise in the same mode at different L^*, and bubbles of the same L^* may rise in the same modes when they have different sizes. However, when both the size and the L^* do not change, different modes may also appear. Fig. 6 shows four basic modes with different styles that can occur when the d_{eq} is 3.10 mm, L^*=3.23. Related parameters are shown in Table 3. As pointed out by previous studies [16,22], the wall effect can reduce the rise velocity of the bubble. And the rise velocity of the bounc-

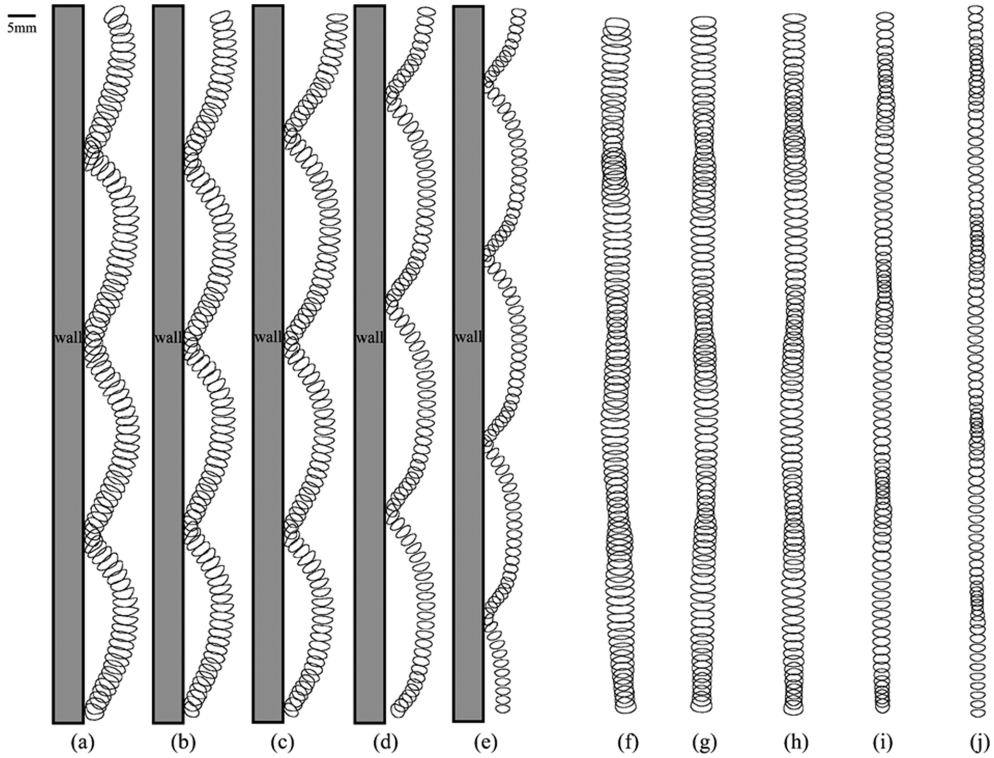

Fig. 5. Bubble migration in the same mode with different sizes. (a)-(e), the results in x-z plane, (f)-(j) the results in y-z plane. For (a) and (f), d_{eq}=2.27; for (b) and (g), d_{eq}=2.49; for (c) and (h), d_{eq}=2.89; for (d) and (i), d_{eq}=3.10; for (e) and (j), d_{eq}=3.40.

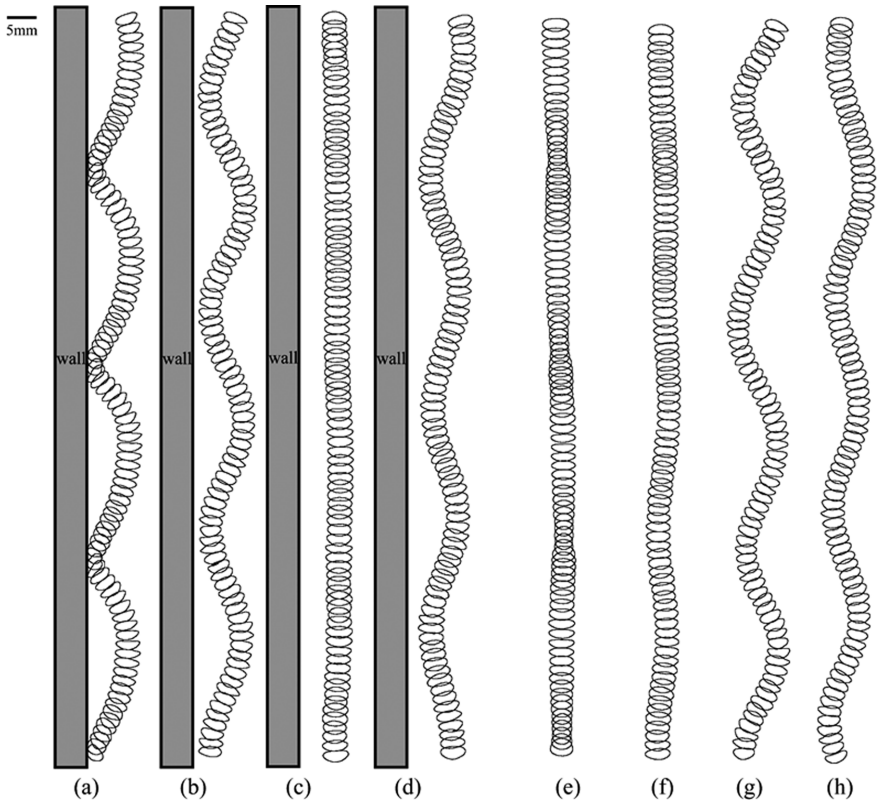

Fig. 6. Bubble migration in different modes. (a)-(d), the results in x-z plane, (e)-(h) the results in y-z plane. For (a) and (e), bubble migration in Mode 1; for (b) and (f), bubble migration in Mode 2; for (c) and (g), bubble migration in Mode 3; for (d) and (h), bubble migration in Mode 4.

Table 3. Parameters of bubble migration in different modes

Mode	$\overline{\lambda}^*$	$\overline{h}^*$	$\overline{d}_{eq}$	$\overline{Re}$	$\overline{We}$	$\overline{u}$
Mode 1	10.75	1.97	3.10	794.14	2.88	0.26
Mode 2	11.89	1.88	3.10	871.48	3.45	0.29
Mode 3	12.16	1.90	3.10	873.34	3.45	0.29
Mode 4	12.32	1.32	3.10	874.09	3.46	0.29

ing bubble is more significantly affected by the wall. Moreover, there is the transmission of surface energy to kinetic energy across the collision, which increases the amplitude [23]. Therefore, the bubble migration in Mode 1 has a larger $\overline{h}^*$ and a smaller $\overline{\lambda}^*$, while that of the other three modes is opposite to that of Mode 1. The $\overline{Re}$, $\overline{We}$, and $\overline{u}$ of bubble migration in Mode 1 are smaller than those of other modes.

In all the results, only at a certain L^*, more than one mode will appear at the same time. For bubbles with a diameter of 3.10 mm, when $L^*<3.23$, only Mode 1 can be observed. When $3.23\le L^*<5.81$, one of the four modes may appear. With the increase of L^*, the frequency of Mode 1 decreases until it does not appear. Then the bubbles mainly rise in Mode 2 and Mode 3. As L^* continues to increase, the frequency of Mode 2 and Mode 3 decreases, and the frequency of Mode 4 increases. When $L^*=5.81$, Mode 4 becomes dominant. When $L^*>8.0$, according to the condition proposed by Krishna et al. [22] ($r_{eq}/L<0.125$), the wall effect is considered negligible.

A similar situation exists for bubbles of other sizes, but the critical L^* has changed. Thus, all bubbles mainly rise in Mode 1 when L^* is small, but other modes will appear at a smaller L^* for larger bubbles. In addition, some non-periodic results are observed at the certain L^*. For example, a bubble has risen a certain distance by Mode 1, then it may rise by Mode 2 later. This is considered as a combination of different modes. The conversion mechanism between different modes is affected by more factors. In this work, only the four basic modes are considered.

The criterion of the mode is the distance between the bubble centroid and the wall (H). The behavior of the bubbles is related to the d_{eq}, u, ρ_g, ρ_l, μ_l, σ and L. In general, it is assumed that the density and viscosity of gas are much smaller than that of liquid ($\rho_g \ll \rho_l$ and $\mu_g \ll \mu_l$). Therefore, it can be predicted that H is a function of the other parameters:

$$H = f(L, d_{eq}, u, \sigma, \mu_l, \rho_l) \tag{10}$$

where u is the bubble velocity and σ is the surface tension between the fluid and the bubble. According to the dimensional analysis, the following equation can be obtained using the Buckingham theory [24]:

$$\frac{2H}{d_{eq}} = K\left(\frac{2L}{d_{eq}}\right)^A \left(\frac{\rho_l U d_{eq}}{\mu_l}\right)^B \left(\frac{\rho_l U^2 d_{eq}}{\sigma}\right)^C \tag{11}$$

That is,

$$H^* = f(L^*, Re, We) \tag{12}$$

Eq. (12) means that the H^* is a function of L^*, Re, and We.

To quantitatively discuss the effects of the above parameters, nonlinear fittings are performed on the results of different modes. The fast Fourier transform is performed on the Re and We to remove the influence of the noise [25,26]:

$$X[k] = \sum_{n=0}^{N-1} x_n e^{-i2\pi kn/N} \tag{13}$$

The results are filtered by the low-pass filter:

$$H(i, j) = \begin{cases} 1, D(i, j) \le D_0 \\ 0, D(i, j) > D_0 \end{cases} \tag{14}$$

where D_0 represents the radius of the passband:

$$D(i, j) = \sqrt{\left(i - \frac{P}{2}\right)^2 + \left(j - \frac{Q}{2}\right)^2} \tag{15}$$

The filtering results are inversed by the discrete Fourier transform:

$$x_n = \frac{1}{N}\sum_{k=0}^{N-1} X[k] e^{i2\pi kn/N} \tag{16}$$

By a nonlinear fitting on experimental data, the correlations which involve Re, We and L^* are proposed, and presented below. Bubbles rising in different modes have different correlations. For bubbles rising in Mode 1:

$$H^* = \varphi \ln(Re) - \psi\sqrt{We} - \xi \tag{17}$$

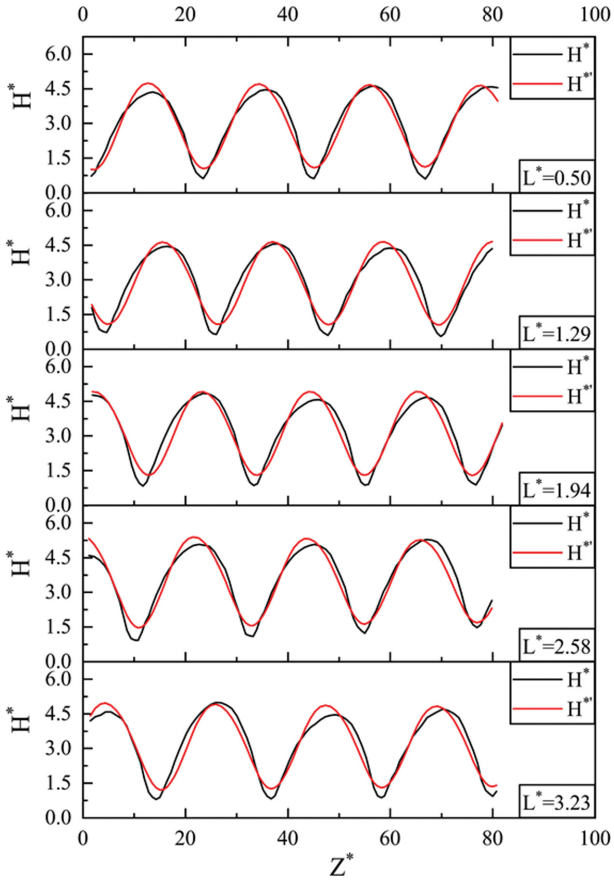

Fig. 7. Comparison of experimental and calculated values of H^* under different L^*.

where

$$\varphi=\frac{121.5-224.35L^{*}+46.82L^{*2}+205.78L^{*3}-192.3L^{*4}+51.68L^{*5}}{1-1.9L^{*}+0.663L^{*2}+1.14L^{*3}-1.15L^{*4}+0.31L^{*5}} \quad (18)$$

$$\psi=\frac{2.8+424.88L^{*}-1{,}194.2L^{*2}+1{,}207.71L^{*3}-182.45L^{*4}-376.84L^{*5}+156.96L^{*6}}{1-0.51L^{*}+0.034L^{*2}-3.05L^{*3}+7.95L^{*4}-6.92L^{*5}+1.9838L^{*6}}\varphi \quad (19)$$

$$\xi=\frac{5.731+7.434L^{*2}+9.23L^{*4}+5.46L^{*6}+2.9L^{*8}}{1+1.297L^{*2}+1.622L^{*4}+0.96L^{*6}+0.509L^{*8}}\varphi \quad (20)$$

The result is shown in Fig. 7. H^* is the dimensionless result of H, and $H^{*'}$ is the calculated value of H^*. Z^* is the dimensionless height of the bubble, which is calculated by $Z^*=2Z/d_{eq}$. For different initial distances, H^* and $H^{*'}$ in the Mode 1 are in good agreement. All correlation coefficients of the measured and calculated values are greater than 0.9, which can be calculated by:

$$r(H^*, H^{*'})=\frac{Cov(H^*, H^{*'})}{\sqrt{Var[H^*]Var[H^{*'}]}} \quad (21)$$

Therefore, Eq. (17) can predict well the H^* in Mode 1. In addition, the influence of L^* on the migration in Mode 1 is indirect. With the increase of L^*, although the coefficient in Eq. (17) shows a regular trend, the wavelength and amplitude of the migration do not fluctuate significantly, which is consistent with Table 1.

The recent simulation results of the deformed bubble rising near the wall show that the oscillation of the bubble is insensitive to the initial distance when the bubble does not collide with the wall [10]. This is consistent with the results of the current work. Comparing the results of different modes, it is found that except Mode 1, L^* has little effect on other modes, and no obvious correlation is found between H^* and Re and We. Considering that H^* is closely related to the bubble migration, the velocity components in the migration direction are defined as the characteristic velocities of the migration Reynolds number (Re_m) and the migration Weber number (We_m):

$$Re_m=Re\frac{u_x}{u} \quad (22)$$

$$We_m=We\frac{u_x^3}{u^2|u_x|} \quad (23)$$

Due to the periodic change of the velocity direction in the process of bubble migration, the bubble velocity has a negative value, and Re_m and We_m are corrected:

$$Re_{mf}=Re_m-(Re_m)_{min} \quad (24)$$

$$We_{mf}=We_m-(We_m)_{min} \quad (25)$$

The correlations of H^* in Mode 2, Mode 3 and Mode 4 are as follows:

$$H^*=12.31+0.038Re_{mf}-24.79We_{mf}+4.37We_{mf}^2-1.99We_{mf}^3+0.34We_{mf}^4 \quad (26)$$

$$H^*=\frac{4.323-3.124Ln(Re_{mf})+0.7664(Ln(Re_{mf}))^2-280.87We_{mf}}{1-0.7197Ln(Re_{mf})+0.1753(Ln(Re_{mf}))^2-63.41We_{mf}-11.32We_{mf}^2} \quad (27)$$

$$H^*=\frac{9.45-0.177Re_{mf}-124.084We_{mf}^2-23.83We_{mf}^2+6.25We_{mf}^3}{0.0374Re_{mf}-14.72We_{mf}-19.684We_{mf}^2+7.565We_{mf}^3-1} \quad (28)$$

The results are shown in Fig. 8. The calculated and experimental values are highly correlated in different modes. The r (H^*, $H^{*'}$) is 0.87 in Mode 3, while it is greater than 0.9 in all other modes. Because the migration in Mode 3 has a smaller amplitude along the wall normal, and it is more sensitive to perturbations.

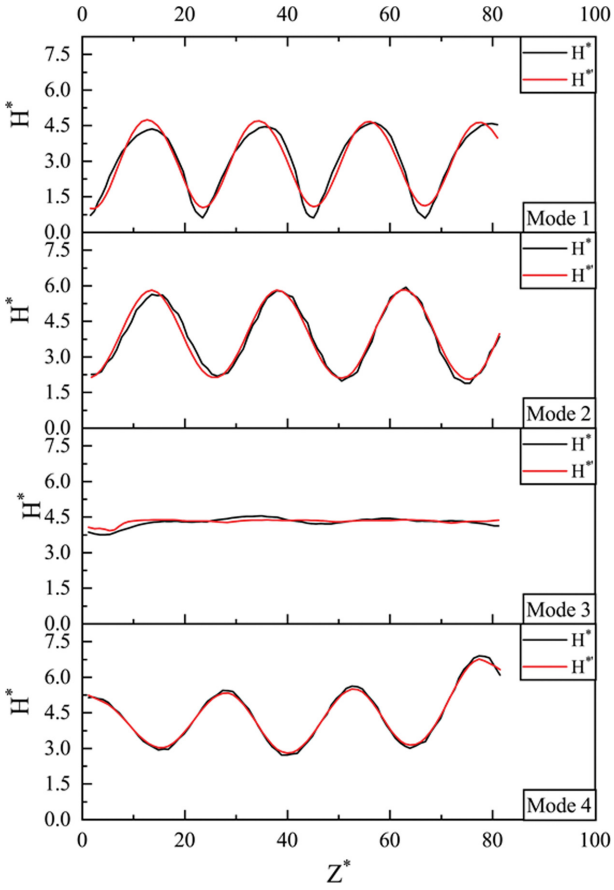

Fig. 8. Comparison of experimental and calculated values of H^* in different modes.

3. The Characteristics of Bubble Migration in Different Modes

As mentioned, the migration of bubbles in the same mode has high similarity, while there are obvious differences in different modes. For bubbles in different modes, some qualitative conclusions can be obtained through the parameters in Table 3. For Mode 1, the $\overline{Re}$ and the $\overline{\lambda}^*$ are significantly smaller than those of other modes, while the $\overline{h}^*$ is slightly larger than that of other modes. This is because Re is mainly affected by the u in the current conditions, and $\overline{\lambda}^*$ is directly related to the u_z. The $\bar{u}$ of the bubble in Mode 1 is 0.26 m/s, while that of the bubble in other modes is 0.29 m/s. Fig. 10 shows that u_z and u have a high similarity. It is not surprising that the Re and $\overline{\lambda}^*$ of Mode 1 are smaller than those of other modes.

However, there is no difference in the average velocity of other modes, which cannot explain the difference of their $\overline{h}^*$. Therefore, the velocity variation of bubbles in different modes needs to be analyzed. In addition, the increase in the amplitude of the bubbles in Mode 1 is the result of the collision. The surface energy stored by the bubble deformation is converted into kinetic energy during the collision process, which compensates part of the kinetic energy loss [16]. The mutual conversion between the surface energy and

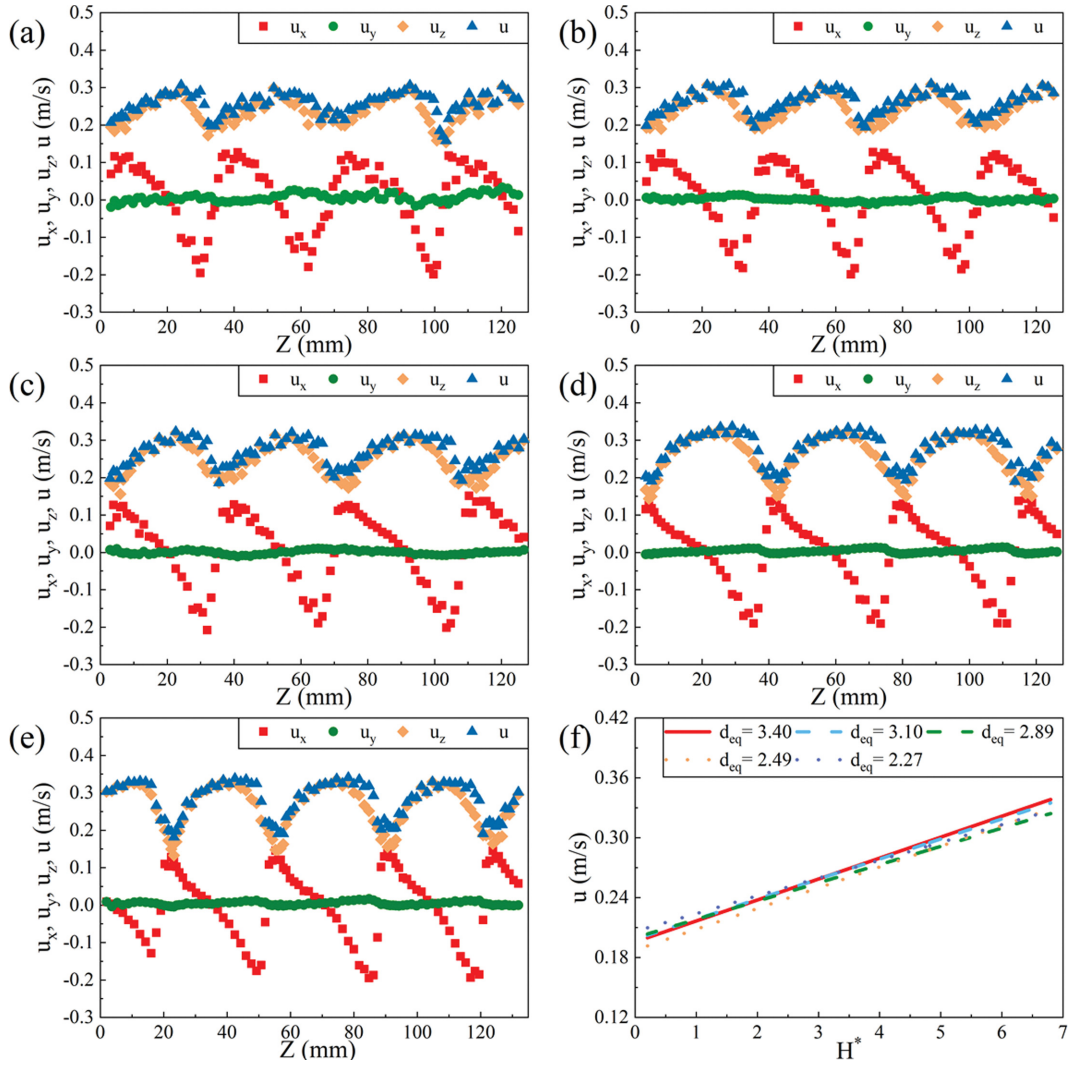

Fig. 9. (a)-(e) The velocity components of bubbles of different sizes rising in the same mode, where (a) d_{eq}=3.40, (b) d_{eq}=3.10, for (c) d_{eq}=2.89, (d) d_{eq}=2.49, (e) d_{eq}=2.27; (f) linear fitting of the relationship between u of bubbles with different sizes and H^*.

the kinetic energy of the bubble is more thorough, compared to the other modes. This can also be confirmed by the evolution of the velocity component u_x along the x direction.

Based on the work of de Vries [14], the bouncing of bubbles along vertical walls in pure water is related to the velocity component. For bubbles rising near a wall, Mode 1 is the most affected by the wall. The local velocity components of bubbles with different sizes in Mode 1 are shown in Fig. 9(a)-(e). Fig. 9(f) is the linear fitting of the relationship between the u and H^*. The wall effect reduces the bubble velocity, and the rising velocity of different bubbles decreases with the decrease of H^*, which is consistent with the conclusion of Krishna et al. [22]. The u_x range of all bubbles is roughly the same. The difference is that the distribution of larger bubbles is more uniform. For smaller bubbles, u_x changes more rapidly from the minimum to the maximum, which indicates that the wall has a more significant impact on the small bubbles. The u_y of all bubbles fluctuates around 0. The u_y of larger bubble shows more obvious velocity pulsation, which is caused by the more severe deformation of the larger bubbles. For smaller bubbles, the pulsation range of u and u_z is larger, which is obviously the result of the wall effect.

For bubbles in the same mode, although the size has a certain influence, the trend is consistent. For bubbles in different modes, the differences are obvious. The components of the same-size bubbles (d_{eq}=3.10 mm) in all basic modes are shown in Fig. 10. The u of bubbles in Mode 1 has obvious periodicity, while the u of bubbles in other modes fluctuates around the average value of 0.29. For all bubbles, the values of u_z and u are close and have a relatively consistent trend, which shows that the main contribution of u comes from u_z. The u_y of bubbles in Mode 1 and Mode 2 is roughly zero. The u_x of bubbles in Mode1 and Mode2 changes periodically. The difference is that the u_y in Mode 2 pulsates slightly, while the u_x in Mode 1 changes faster from the minimum to the maximum. Obviously, the bubbles in Mode 1 are more constrained by the wall. The changes of u_x and u_y in Mode 3 are opposite to that in Mode 2. The u_x in Mode 3 is basically zero. The u_y in Mode 3 changes periodically. Note that compared with u_y in Mode 2, u_x of the bubble in Mode 3 is more stable. As is known, the wake plays an important role in the bubble motion. When the bubble is unbounded,

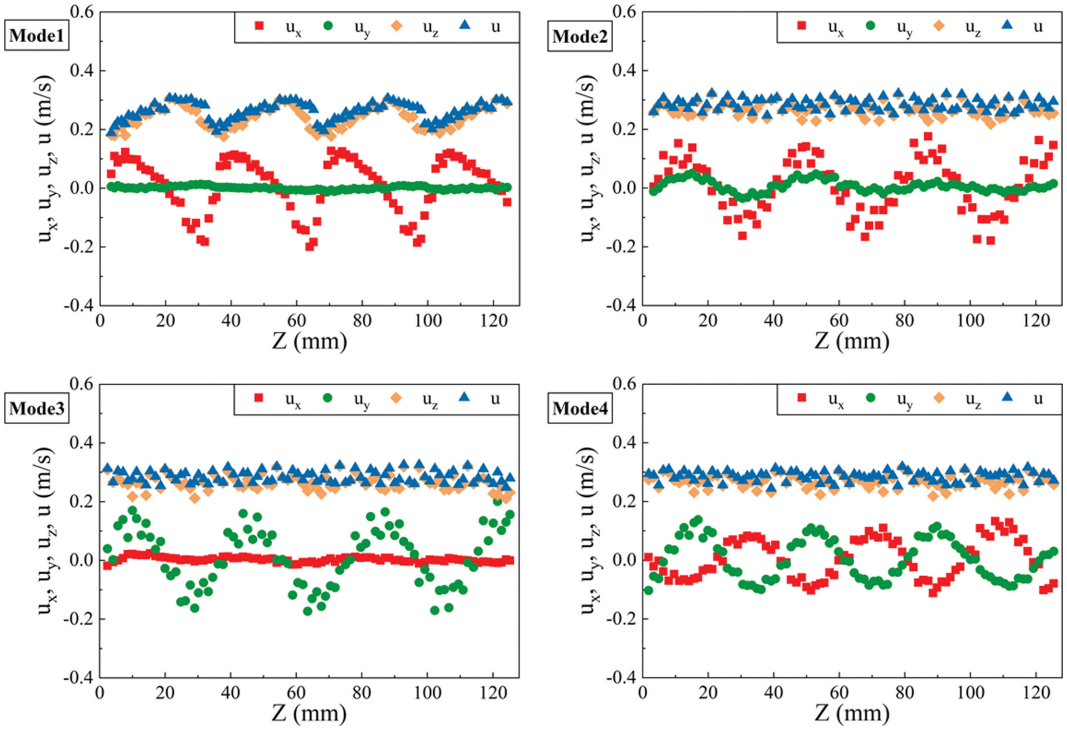

Fig. 10. The velocity components of the bubble rising in different modes.

there are alternately shedding hairpin vortices in the wake of the bubble with zigzag trajectory, and there are intertwined double helical vortices in the wake of the bubble with spiral trajectory [27]. When a wall exists, the wall effect can inhibit the near wall side vortex shedding, which induces the wall normal transverse force [28]. Obviously, in Mode 3, the hairpin vortex sheds along the wall spanwise, and the inhibiting effect remains constant. On the other hand, in Mode 2, the hairpin vortex sheds in the wall normal direction, and the inhibiting effects changes. Accordingly, the u_x in Mode 3 is more stable than the u_y in Mode 2. The wall effect can also be found in Mode 4. Due to the constraint provided by the centripetal force in the helical motion [21], both u_x and u_y in Mode 4 show smaller periodic changes. Considering the wall effect, the peak value of u_x is slightly smaller than the peak value of u_y.

4. The Dynamics of Bubble Migration in Different Modes

The average value cannot reflect the velocity change in the migration process, and the average force cannot reflect the complete force process of the bubble. A reliable way to calculate the force on a bubble is based on generalized Kirchhoff equation [29]. The relationship of the angular velocity, linear velocity of bubbles and the force of bubbles is obtained by [30,31]:

$$\rho V\left(A\cdot\frac{du}{dt}+\Omega\times A\cdot u\right)=F_e \tag{29}$$

$$\rho V\left(D\cdot\frac{d\Omega}{dt}A\cdot\frac{du}{dt}+\Omega\times(D\cdot\Omega)+u\times(A\cdot u)\right)=\Gamma_e \tag{30}$$

where F_e and Γ_e are the external force and torque acting on the bubble; A and D represent the additional mass and rotational inertia tensor respectively; Ω and u are angular velocity and linear velocity of bubble motion, respectively. This equation can calculate the force and torque acting on the bubble according to the bubble velocity. Kong et al. [32] studied the rising behavior of a pair of bubbles in static liquids, and used Eq. (13) to calculate the force change of the bubbles. The boundary conditions in the current work are similar to those in their work, so the method is also suitable for this work.

For ellipsoidal bubbles, it is generally considered that the short axis direction is consistent with the velocity vector [19,33,34]. Therefore, Eq. (12) and Eq. (13) can be simplified to:

$$\rho V A_{11}\frac{du}{dt}=F_D+F_{B1},\ \rho V\Omega_3 A_{11}u=F_{L2}+F_{B2},\ \rho V\Omega_2 A_{11}u=F_{L3} \tag{31}$$

$$\Omega_1=\frac{d\phi}{dt}\cos\theta,\ \Omega_2=\frac{d\phi}{dt}\sin\theta,\ \Omega_3=-\frac{d\theta}{dt},$$
$$d\phi/dt=\left(u_x\frac{du_y}{dt}-u_y\frac{du_x}{dt}\right)/(u_x^2+u_y^2) \tag{32}$$

$$F_{B1}=\rho Vg\cos\theta,\ F_{B2}=\rho Vg\sin\theta,\ \theta=\arctan(u_x/u_z) \tag{33}$$

where θ is the pitch angle of the path and ϕ is the azimuthal angle between a fixed horizontal line and the horizontal projection of the 1-direction (Fig. 11). A_{11} is the additional mass tensor, which can be calculated by the shape function of the bubble:

$$A_{11}=\frac{\alpha}{2-\alpha} \tag{34}$$

$$\alpha=\frac{2}{1-\chi^{-2}}\left[1-\frac{\chi^{-2}}{\sqrt{1-\chi^{-2}}}\arcsin\sqrt{1-\chi^{-2}}\right] \tag{35}$$

Drag coefficient (C_D) and lift coefficient (C_L) of the rising bubbles are calculated by:

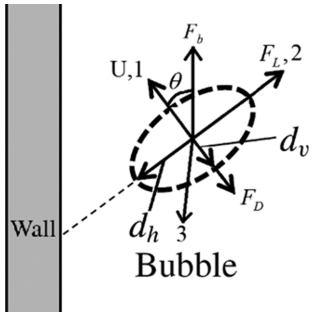

Fig. 11. Schematic diagram of bubble migration near a wall.

$$C_D = F_D/(\pi r_{eq}^2 \rho U^2/2),\ C_L = F_L/(\pi r_{eq}^2 \rho U^2/2) \quad (36)$$

Fig. 12 shows the relationship between the C_D and Re in the current work, which is compared with that in Clift's work [35]. According to the research of Clift [35], the C_D of the rising bubble in the cylinder is:

$$C_D = C_{D\infty} + 24/\mathrm{Re}(K-1) \quad (37)$$

where $K=1/(1-1.6\delta^{1.6})$; $\delta \le 0.6$; δ=d/D; d and D are the diameters of the bubble and the cylinder, respectively. The larger δ indicates that the bubble is more affected by the wall. The dotted lines of different colors are the results from Clift's work [35], which are under current working conditions. The solid lines of different colors in Fig. 12(a). are the fitting curves of the C_D of bubbles with different sizes. The solid lines in Fig. 12(b) are the fitting curves of the C_D of bubbles in different modes. According to the dotted lines, when the Re is constant, as the wall influence weakens, the C_D decreases. It can be found that the trend of the dotted line is gentler. C_D is a decreasing function of the Re. When Re increases to a certain range, the C_D tends to be constant. Obviously, the decrease of C_D increases the u of bubbles. Re is a positive, where $K=1/(1-1.6\delta^{1.6})$; $\delta \le 0.6$; δ=d/D; d and D are the diameters of the bubble and the cylinder, respectively. The larger δ indicates that a bubble is more affected by the wall. The dotted lines of different colors are the results from Clift's work [35], which are under current working conditions. The solid lines of different colors in Fig. 12(a) are the fitting curves of the C_D of bubbles with different sizes. The solid lines in Fig. 12(b) are the fitting curves of the C_D of bubbles in different modes. According to the dotted lines, when the Re is constant, as the wall influence weakens, the C_D decreases. It can be found that the trend of the dotted line is gentler. The C_D is a decreasing function of the Re. When Re increases to a certain range, C_D tends to be constant. Obviously, the decrease of C_D increases the u of bubbles. Re is a positive correlation function of u. When C_D decreases to a certain extent, the influence on bubble velocity can be ignored. For bubbles of different sizes, as Re increases, C_D decreases at a similar rate. And under the same Re, C_D of larger-size bubbles is greater.

For bubble rising in different modes, the variation of C_D with the Re is different. When Re is small, C_D of bubbles in different modes is closer to the result of Clift's work [35]. When δ>0.4, the results from Clift's work [35] are greater than the current calculation result. This is because the bubble is more affected by the wall when it is close to the wall. So, its velocity is small, and Re is small. When the bubble is far from the wall, it is weakly affected by the wall. So, the velocity is larger, and Re is correspondingly larger. As Re increases, C_D of the bubble in Mode 1 decreases more slowly than that in other modes due to the greater wall constraints. In addition, the trend of C_D changing with Re in Mode 2 and Mode 3 is roughly the same, but C_D in Mode 3 decreases more slowly than that of Mode 2. C_D of Mode 4 is initially smaller than that of Mode 2 and Mode 3. But C_D curves of Mode 4 gradually flatten, and finally C_D of Mode 4 is greater than that of Mode 2 and Mode 3.

The trends of the C_D and C_L can better explain the influence of the wall. The results are shown in Fig. 13. In Mode 1, C_D and C_L show regular periodicity due to the limitation of the wall. However, the extreme values of C_D and C_L in Fig. 13(a) do not exactly correspond to the extreme values of H^*. C_D reaches its peak value after the bubble collides with the wall and moves away a short distance. And C_D reaches the valley value after moving towards the wall for a short distance at the farthest point from the wall. C_L peaks at a short distance before the collision, and reaches the val-

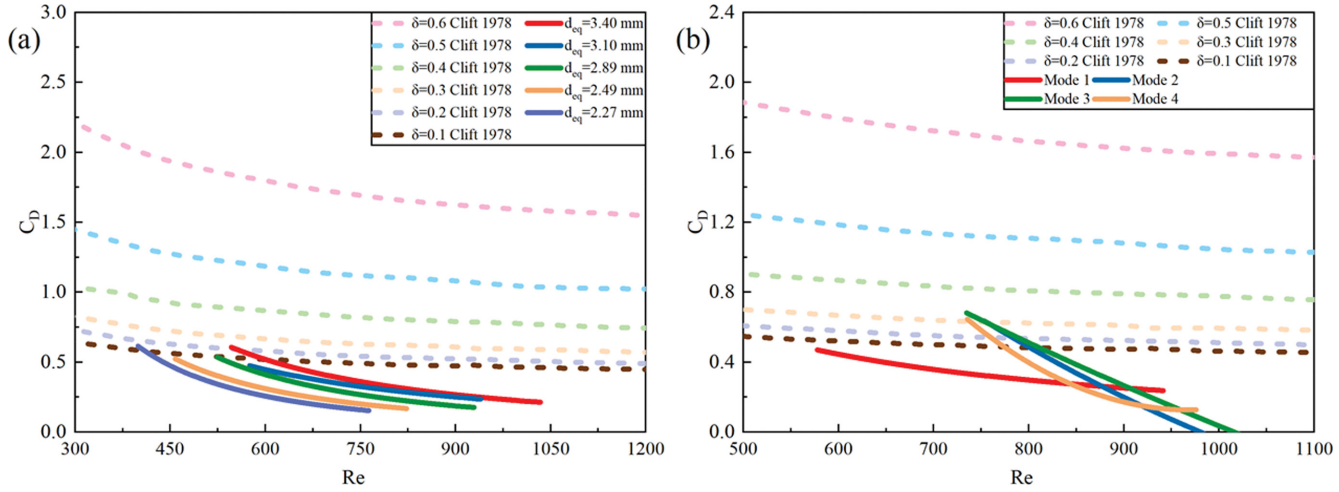

Fig. 12. The relationship between the C_D and the Re, which is compared with the result of Clift. (a) The C_D of different sizes of bubble rising in Mode 1. (b) The C_D of the same size bubble (d_{eq}=3.10) in different modes.

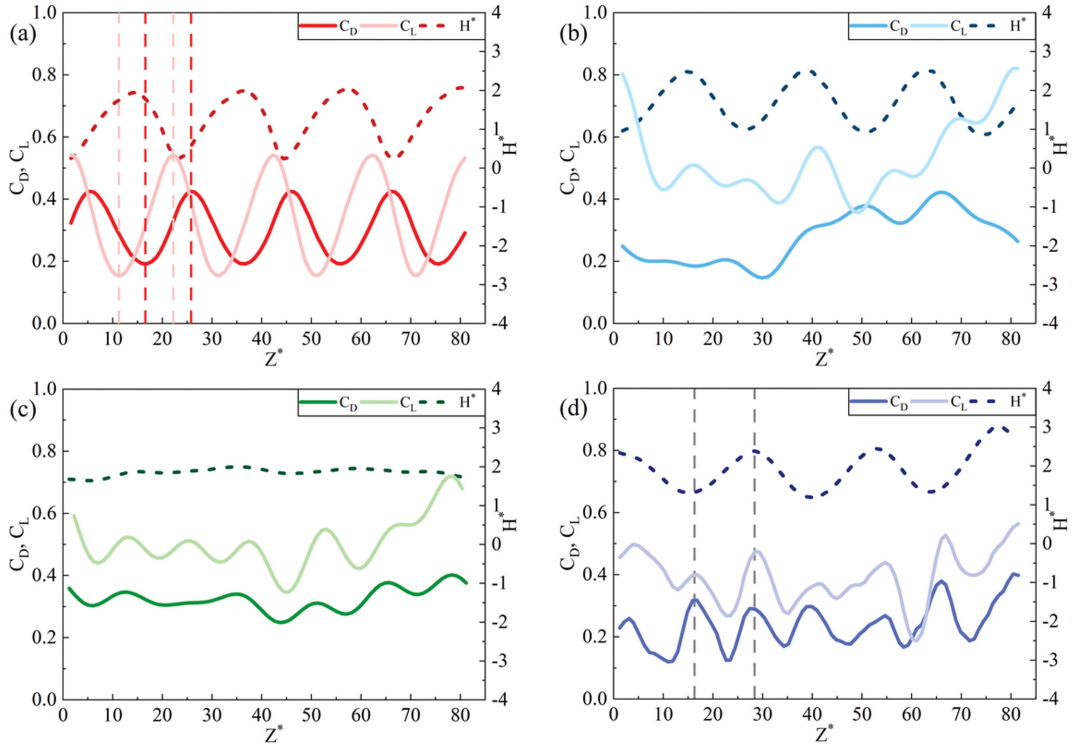

Fig. 13. The C_D and the C_L of bubble rising in different modes; (a) in Mode 1; (b) in Mode 2; (c) in Mode 3; (d) in Mode 4.

ley at a short distance before the furthest distance from the wall. The wall effect can cause an increase in velocity fluctuations, which in turn causes a change in the drag coefficient [15,36]. This is consistent with the results of different modes of bubble motion in the current work. For bubbles bouncing along the wall, the normal rebound velocity is greater than the approach velocity. And when the Reynolds number is high enough, the lift force pushes the bubble close to the wall, and drag prevents the bubble from moving away from the wall [36,37]. This is why the peaks of C_D and C_L in Mode 1 are shifted. For Mode 2 and Mode 3, C_D and C_L do not have the periodicity like Mode 1 due to the weakened wall effect. Considering the effect of the wall on the velocity components of different modes, which is mentioned in Section 3.3, it is not surprising that C_D and C_L are more stable in Mode 3 than in Mode 2. For Mode 4, the periodicity of C_D and C_L is not as obvious as that of Mode 1, but they have better consistency with the bubble motion. Moreover, C_D and C_L are smaller in Mode 4 than in other modes. For a spirally rising bubble, the lift component along the normal direction provides the centripetal force for circular motion, and the lift component along the bi-normal direction provides the power for migration [21]. The periodicity of Mode 4 is the result of the constraint of the normal-direction lift component. Furthermore, the migration force provided by the lift force is reduced due to the constraints provided in the normal direction. As a result, the amplitude in Mode 4 is smaller, and C_D and C_L are correspondingly smaller than other modes.

CONCLUSIONS

The migration of deformable bubbles near a vertical wall in pure water was studied using the dual-camera orthogonal shadow method. The influence of different size ($2.27\ \text{mm} \le d_{eq} \le 3.40\ \text{mm}$) and different initial distance ($0.5 \le L^* \le 3.5$) on migration was discussed. The results show that the effect of size and initial distance is indirect. The same mode appears for different initial distances and sizes. But for the same initial distance and size, different modes may also appear. The dimensionless initial distance, Reynolds number, and Weber number together determine the migration mode. The size and initial distance can affect the frequency of different modes.

Four basic migration modes are summarized, and the kinematic and dynamic characteristics of different modes are discussed. New correlations based on dimensionless initial distance, Reynolds number, and Weber number are proposed to predict bubble migration in different modes near the wall. The migration characteristics of different modes are significantly different. Previous studies confirmed that the wall effect can inhibit the velocity of rising bubbles. The bubbles in mode 1 are most affected by the wall, and the rising velocity has obvious periodic fluctuations. For the other modes, the influence of the wall is mainly expressed in the velocity component, and there is no obvious difference in the total velocity. Due to the wall effect, the velocity along the migration normal in mode 3 is more stable than in mode 2, while the velocity component along the wall normal in mode 4 is less than the wall spanwise. Accordingly, bubbles in different modes have different dynamic characteristics. The trend of the drag coefficient decreasing with Reynolds number is consistent with the results of previous studies on cylindrical containers, and the decrease in Mode 1 is more gradual than that in other modes. Due to the difference in velocity between approaching and moving away from the wall, C_D and C_L in Mode 1 have peak shifts that do not exist in other modes. Mode 4

has a smaller C_D and C_L than the other modes because lift provides a constraint along the motion normal. It is expected that the results can help to predict and control the bubble distribution and gas holdup, and to improve the reaction efficiency for chemical process equipment, such as a bubble column.

ACKNOWLEDGEMENTS

This research was supported by the National Natural Science Foundation of China (11572357, 11602077).

NOTES

The authors declare no competing financial interest.

NOMENCLATURE

L : initial distance [mm]
d_{eq} : equivalent diameter [mm]
d_h : horizontal axis of in a plane of the bubble [mm]
d_v : vertical axis of in a plane of the bubble [mm^2]
u : bubble velocity [m/s]
Δt : time interval [s]
H : instant wall distance [mm]
λ : migration wavelength [mm]
h : migration amplitude [mm]
Re : bubble Reynolds number [-]
We : bubble Weber number [-]
σ : surface tension [N/m]
μ : viscosity [Pa·s]
ρ : density [kg/m^3]
r : correlation coefficient [-]
Re_m : migration Reynolds number [-]
We_m : migration Weber number [-]
F_D : drag force [N]
F_L : lift force [N]
C_D : drag coefficient [-]
C_L : lift coefficient [-]

Subscripts

x : in x-direction
y : in y-direction
z : in z-direction
i : frame sequence
g : gas phase
l : liquid phase

Superscripts

* : dimensionless

REFERENCES

1. R. O. Meehan, B. Donnelly, K. Nolan and D. B. Murray, *Int. J. Heat Mass Tran.*, **108**, 1347 (2017).
2. H. Maeng and H. Park, *Int. J. Heat Mass Tran.*, **165**, 120590 (2021).
3. J. Yin, Y. Zhang, J. Zhu, L. Lv and L. Tian, *Int. J. Heat Mass Tran.*, **17710**, 121525 (2021).
4. L. Liu, H. Yan and G. Zhao, *Exp. Therm. Fluid Sci.*, **62**, 109 (2015).
5. J. Magnaudet and I. Eames, *Annu. Rev. Fluid Mech.*, **321**, 659 (2000).
6. A. Tomiyama, G. P. Celata, S. Hosokawa and S. Yoshida, *Int. J. Multiph. Flow*, **289**, 1497 (2002).
7. X. Yan, K. Zheng, Y. Jia, Z. Miao, L. Wang, Y. Cao and J. Liu, *Ind. Eng. Chem. Res.*, **57**, 5385 (2018).
8. F. Suñol and R. González-Cinca, *Int. J. Multiph. Flow*, **113**, 191 (2019).
9. H. Maeng and H. Park, *Int. J. Heat Mass Tran.*, **165**, 120590 (2020).
10. Y. Zhang, S. Dabiri, K. Chen and Y. You, *Int. J. Heat Fluid Flow*, **85**, 108649 (2020).
11. J. Yuan, Z. Weng and Y. Shan, *Int. J. Therm. Sci.*, ***1686***, 107037 (2021).
12. Q. Yu, X. Ma, G. Wang, J. Zhao and D. Wang, *Ultrason. Sonochem.*, **71**, 105396 (2020).
13. Z. P. Li, L. Q. Sun, W. Xiao and X. L. Yao, *Ocean. Eng.*, **186**, 106066 (2019).
14. A. W. G. de Vries, University of Twente (2001).
15. M. F. Moctezuma, R. Lima-Ochoterena and R. Zenit, *Phys. Fluids*, **179**, 098106 (2005).
16. H. Jeong and H. Park, *J. Fluid Mech.*, **771**, 564 (2015).
17. J. Lee and H. Park, *Int. J. Multiph. Flow*, **91**, 225 (2017).
18. Y. Chen, C. Tu, Q. Yang, Y. Wang and F. Bao, *Exp. Therm. Fluid Sci.*, **120**, 110235 (2020).
19. A. W. G. de Vries, A. Biesheuvel and L. v. Wijngaarden, *Int. J. Multiph. Flow*, **2811**, 1823 (2002).
20. F. Takemura and J. Magnaudet, *J. Fluid Mech.*, **495**, 235 (2003).
21. C. Veldhuis, University of Twente (2007).
22. R. Krishna, M. I. Urseanu, J. M. V. Baten and J. Ellenberger, *Int. Commun. Heat Mass*, **266**, 781 (1999).
23. A. Zaruba, D. Lucas, H.-M. Prasser and T. Höhne, *Chem. Eng. Sci.*, **626**, 1591 (2007).
24. Y. Nakayama, *Introduction to fluid mechanics (Second Edition)*, Butterworth-Heinemann (2018).
25. M. H. Hayes, *Schaum's outline digital signal processing*, McGraw-Hill Companies (1999).
26. S. K. Mitra, *Digital signal processing: A computer-based approach*, McGraw-Hill Companies (2005).
27. C. Brucker, *Phys. Fluids*, **117**, 1781 (1999).
28. L. Zeng, S. Balachandar and P. Fischer, *J. Fluid Mech.*, **536**, 1 (2005).
29. G. Mougin and J. Magnaudet, *Int. J. Multiph. Flow*, **2811**, 1837 (2002).
30. W. L. Shew, S. Poncet and J. F. Pinton, *J. Fluid Mech.*, **569**, 51 (2006).
31. W. L. Shew and J. F. Pinton, *Phys. Rev. Lett.*, **9714**, 144508 (2006).
32. G. Kong, H. Mirsandi, K. Buist, E. Peters, M. Baltussen and J. Kuipers, *Exp. Fluids*, **6010**, 155 (2019).
33. G. Mougin; J. Magnaudet. *Phys. Rev. Lett.*, **881**, 014502 (2002).
34. K. Ellingsen and F. Risso, *J. Fluid Mech.*, **440**, 235 (2001).
35. R. Clift, J. R. Grace and M. E. Weber, *Bubbles, drops, and particles*, Academic Press (1978).
36. B. Figueroa-Espinoza, R. Zenit and D. Legendre, *J. Fluid Mech.*, **616**, 419 (2008).
37. F. Takemura, S. Takagi, J. Magnaudet and Y. Matsumoto, *J. Fluid Mech.*, **461**, 277 (2002).